Measuring the Stiffness and Coherence Length of 2D Superconductors

Nitsan Blau

Measuring the Stiffness and Coherence Length of 2D Superconductors

Research Thesis

In Partial Fulfillment of The Requirements for the
Degree of Master of Science in Physics

Nitsan Blau

Submitted to the Senate of the Technion - Israel
Institute of Technology

Tevet, 5780, Haifa, January, 2020

The Research Thesis was done under the supervision of
Professor Amit Keren in the Department of Physics.

The generous financial help of the Technion is
gratefully acknowledged.

Contents

List of Figures

Abstract

The gauge-invariant London equation $\boldsymbol{J_s} = -\rho_s \left(\boldsymbol{A} - \frac{\hbar}{2e}\boldsymbol{\nabla}\phi\right)$ states that the current density in a superconductor (SC) $\boldsymbol{J_s}$ is proportional to the vector potential $\boldsymbol{A}$ up to the gradient of the order parameter phase ϕ. The proportionality constant ρ_s is called the stiffness which is connected to the penetration depth λ by the relation $\rho_s = \frac{1}{\mu_o \lambda^2}$. When cooling a SC at zero $\boldsymbol{A}$, ϕ will be uniform to minimize the kinetic energy. In cases where ϕ is quantized, it remains uniform upon slightly increasing $\boldsymbol{A}$, leading to the familiar London equation $\boldsymbol{J_s} = -\rho_s\boldsymbol{A}$. This relation holds until $\boldsymbol{J_s}$ reaches a critical current $\boldsymbol{J_c}$ where ϕ is forced to change. The coherence length ξ is proportional to $\frac{1}{\boldsymbol{J_c}}$. The standard procedure for measuring ρ_s in a bulk SC is to apply a magnetic field and measure its penetration depth λ into the interior of the SC. However, in ultra-thin SC films, the penetration depth is not well defined since there is no interior although surface current $\boldsymbol{J_s}$ and $\boldsymbol{A}$ do exist. A new way of measuring the superconducting stiffness and coherence length using a Stiffnessometer was developed [1] in our group. This method measures ρ_s and $\boldsymbol{J_c}$ directly, based on the London equation with a rotor free vector potential. The method, applicable to $3D$ and $2D$ SC, is based on long and narrow excitation coil which pierces a ring-shaped SC and produces a current in the ring. The ring's magnetic moment m is then measured by a superconducting quantum interference device (SQUID) to extract ρ_s and $\boldsymbol{J_c}$ (or the critical SC surface current density $\boldsymbol{\mathcal{J}_c}$ in the $2D$ case). In this work, I will present stiffness and coherence length measurements of a $2D$, ultra-thin $\delta -$ NbN and thin Granular Al SC films. The thinnest film that was measured is a 3[nm] thick NbN film. A surplus of signal to noise ratio (SNR) in this measurement shows that a reduction of factor 10 in the thickness of the samples is possible, a fact that will allow in the future to apply this method on a true $2D$ systems with a single atomic layer. The analysis of the measured signals with the Pearl equation shows that our new method works appropriately and gives similar stiffness values found in the literature. Using full analysis of the two coupled Ginzburg-Landau (GL) equations we extract the coherence lengths which are similar to those available in the literature. Finally, this work demonstrates for the first time that the Stiffnessometer agrees with other techniques while it opens new measurement regimes.

Symbols and Abbreviations

Abbreviations

BC	Boundary Conditions
CP	Cooper Pairs
GL	Ginsburg Landau
HR	High Resistivity
JJE	Josephson Junction Effect
LR	Low Resistivity
PDE	Partial Differential Equation
SC	Superconductor / Superconducting
SNR	Signal to Noise Ratio
SQUID	Superconducting Quantum Interference Device
TI	Topological Insulator
ZGFC	Zero Gauge-Field Cooling

Symbols

$\boldsymbol{A}$	Vector Potential
B	Total Magnetic Field
c	Speed of Light
e	Electron Charge
H	External Magnetic Field
H_{c1}	First Superconducting Critical Field
H_{c2}	Second Superconducting Critical Field
I	Current
$\boldsymbol{J}_s$	Current Density
J_c	Critical Current Density
m	Magnetic Moment

m_e	Electron Mass
n	Windind Density of the Excitation Coil
$\hat{\varphi}$	Azimuthal Direction
Φ	Magnetic Flux
ϕ	Phase of the Complex Order Parameter
Φ_0	Flux Quantum
ψ	Complex Order Parameter
ρ	Resistivity
$\hat{\rho}_s$	Superconducting Stiffness
T	Temperature
T_c	Critical Temperature
v_c	Critical Velocity
ξ	Coherence Length

1 Introduction

1.1 Motivation

The Stiffnessometer is a new measuring device that was developed [1] in our group to measure the superconducting stiffness ρ_s and the coherence length ξ of superconducting materials. The Stiffnessometer technique will be explained in detail in chapter 2. The method is based on a current I passing through a conducting long and narrow excitation coil. In that case, a curl-free (zero magnetic field) vector potential which is proportional to I is formed outside of the coil. The coil pierces a ring-shaped SC and induces a superconducting current density $\boldsymbol{J_s}$ in the ring according to the London equation $\boldsymbol{J_s} = -\rho_s \boldsymbol{A}$. The ring's magnetic moment is then measured by a superconducting quantum interference device (SQUID) to extract ρ_s which is connected to the penetration depth λ by the relation $\rho_s = \frac{1}{\mu_0 \lambda}$. By increasing $\boldsymbol{A}$ until the London equation does not hold anymore we determine the critical current density $\boldsymbol{J_c}$. The coherence length ξ is a property which is directly connected to $\boldsymbol{J_c}$. One can define two regimes when measuring the stiffness of superconducting materials. The first regime is the $3D$ regime which occurs when the penetration depth λ is smaller compared to all dimension of the SC ring, especially to the ring thickness d. In this case, the method is sensitive to very small stiffness, which translates to penetration depths on the order of $\lambda \sim 1\,[\mathrm{mm}]$ and to extremely low critical current densities $\boldsymbol{J_c} \sim 1\left[\mathrm{Acm}^{-2}\right]$ or long coherence lengths $\xi \sim 1\,[\mu\mathrm{m}]$. Those kinds of measurements were demonstrated in the work of Dr. Itzik Kapon [1] on high-temperature SC LSCO compound ($\mathrm{La_{2-x}Sr_xCuO_4}$) which is part of the cuprates family. The second regime is the $2D$ regime, when $\lambda \gg d$. In this case, the penetration depth is not well defined since there is no interior to the sample although surface current $\boldsymbol{\mathcal{J}_s}$ and $\boldsymbol{A}$ do exist. Therefore, it is necessary to define a new length scale when dealing with $2D$ SC - the Pearl length $\Lambda \equiv \frac{\lambda^2}{d}$.

There are two main motivations for this research work. The first one is to approve the new method by showing extraction of absolute SC stiffness values from base temperature all the way to T_c that agrees with other known methods. That couldn't have to be done with a bulk SC sample because in the $3D$ regime, the method sensitivity is limited to penetration depths on the order of the smallest dimension of the sample (as will be shown in section 2.3), i.e. $\lambda \sim 1\,[\mathrm{mm}]$. This leads to saturated measurement (Fig. 1.1a) below T_c when λ is much smaller. Therefore we were encouraged to measure thin film samples.

The second motivation is to examine the ability of the Stiffnessometer to measure ultra-thin SC films as a proof of concept. This is the first step towards

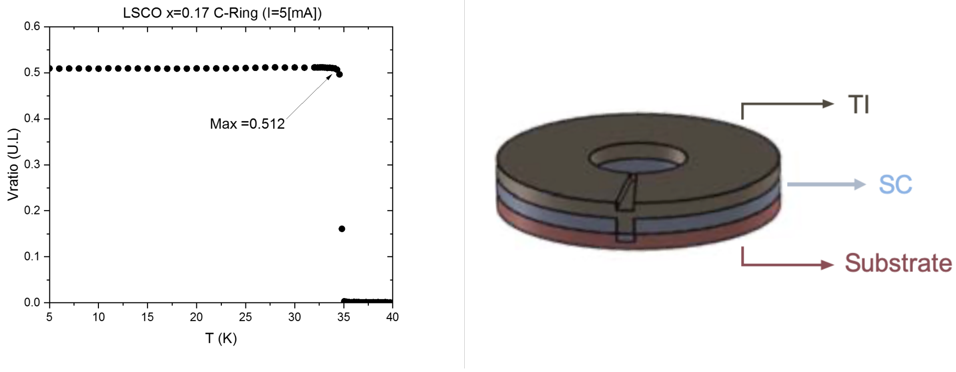

(a) (b)

Figure 1.1: (a) Stiffness measurement of bulk LSCO ring. From the V_{ratio} value, one can extract the stiffness (as will be explained in chapter 2). Below the critical temperature ($T_c = 35\,[\mathrm{k}]$), the measurement value is saturated and the stiffness temperature dependency can't be extracted because its value is out of the sensitivity range of the Stiffnessometer (the penetration depth λ becomes much smaller than any geometrical length of the sample). (b) Illustration of the double-layered SC\TI sample. Having a stiffness signal from such a device will indicate a superconducting surface state that emerges from a SC\TI proximity effect.

a bigger project aimed to look for superconductivity emerging from the surface state of a Topological Insulator (TI). The idea is to fabricate double-layered ring-shaped sample with a close ring TI layer on top of an open ring SC layer (Fig. 1.1b) in such a way that Cooper-pairs (CP) will tunnel from the SC to the conducting surface state of the TI and will form a proximity effect [2]. Upon measuring with the Stiffnessometer, only superconducting close ring will have the ability to run super-currents in a loop and produce a magnetic moment [1], unlike in a standard magnetization measurement where both types of rings will have a detectable magnetic moment as shown in Fig. 1.2. Therefore, having a signal from such a SC\TI device will indicate a TI superconducting surface state.

In this work, I will show that the Stiffnessometer is indeed capable of measuring the Pearl length of ultra-thin $2D$ SC from which one can extract directly the stiffness and the penetration depth. As will be shown in chapter 2, in the $2D$ regime, our method is sensitive to a penetration depth in the range of $\lambda\,[\mathrm{nm}] \in \left(60\sqrt{d}\,,\, 6000\sqrt{d}\right)$ where d is the film thickness given in [nm]. A surplus of SNR in 3[nm] thick NbN film measurement shows that a reduction of factor 10 in the thickness of the samples is possible, a fact that will allow in the

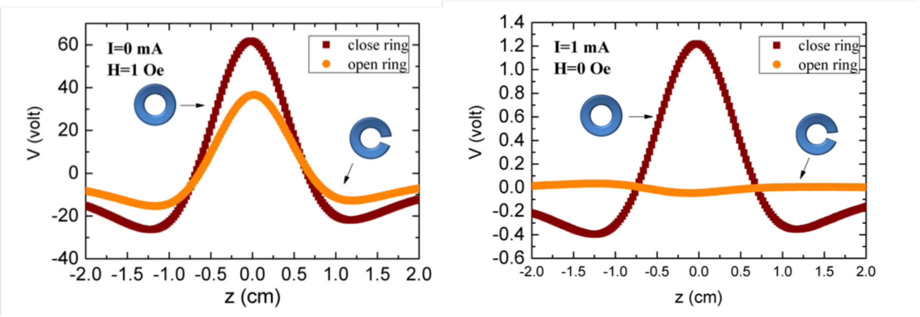

Figure 1.2: The Stiffnessometer is based on a magnetic moment measurement. Both graphs present a comparison between SC close ring (red) and open ring (orange) measurements. The left figure shows a regular magnetic moment measurement of the SC rings in a uniform magnetic field ($H = 1\,[\mathrm{Oe}]$). The signal is due to the diamagnetic response of the SC. The right figure shows a Stiffnessometer measurement with coil current of $I = 1\,[\mathrm{mA}]$. There is a signal only from the close ring which can run super-currents in a loop and produce a magnetic moment while there is no signal from the open ring.

future to apply this method on a truly $2D$ systems such as a TI superconducting surface state.

1.2 Superconductivity

Superconductivity (SC) is a special phase of matter characterized by two main phenomena. the first is zero electrical resistance and the second is the Meissner effect - an expulsion of a magnetic field from the interior of the SC, or in other words, a perfect diamagnetism. Metallic SC can be explained by the BCS theory named after John Bardeen, Leon Cooper, and John Robert Schrieffer. The BCS theory describes an attractive interaction between electrons through electron-phonon coupling which creates CP - a pair of electrons that constitute the charge carriers in the SC. The critical temperature T_c refers to the temperature where the transition between the SC phase and the normal phase happens.

The coherence length ξ can be defined as the size of the CP. In the language of the GL theory, it is defined as the shortest length scale over which the phase of the complex order parameter can vary. In the vicinity of an external magnetic field, the SC will expel the field from its interior by a screening super-currents in such a way that the external field penetrates to the interior of the SC from the interfaces with an exponential decaying on the length scale of λ known as the penetration depth.

There are two types of SC, depending on the ratio between both length scales ξ and λ. Type-I SC have $\lambda < \xi$ and type-II SC have $\lambda > \xi$. A type-I SC will expel all external magnetic field until the field reaches some critical field

H_c. Above it, the material will turn back to its normal phase, allowing all the magnetic flux to penetrate into the interior of the material. Type-II SC will expel the external field up until some critical field H_{c1} which above it, some field lines with quantized flux will penetrate into the SC at discrete sites in the form of vortices. The core of each such vortex is in the normal phase while the outside is still in the SC phase. Increasing the external field above H_{c1} causes more vortices to penetrate into the interior until their density becomes in the order of $\sim 1/\xi^2$ such that they start to overlap. In that case, the entire material becomes normal - that is the second critical field H_{c2}.

1.3 The London Equation and the Meissner Effect

The superconducting Stiffness ρ_s is defined by a local relation between the superconducting current density $\boldsymbol{J}$ to the vector potential $\boldsymbol{A}$ and the gradient of the complex order parameter phase, which is defined as $\psi = |\psi|e^{i\phi}$. The relation is given by the gauge-invariant London equation:

$$\boldsymbol{J_s} = -\rho_s \left(\boldsymbol{A} - \frac{\hbar}{2e} \boldsymbol{\nabla} \phi \right) \tag{1.1}$$

For simplicity, one can assume isotropy, therefore ρ is a scalar (although in the most general case it is a tensor). When $\boldsymbol{\nabla}\phi = 0$ as in our case, we get:

$$\boldsymbol{J_s} = -\rho_s \boldsymbol{A} \tag{1.2}$$

Applying a rotor over Ampere's-Maxwell equation, we get:

$$\boldsymbol{\nabla} \times \boldsymbol{\nabla} \times \boldsymbol{B} = \mu_0 \boldsymbol{\nabla} \times \boldsymbol{J_s}$$

Placing Eq. 1.2 for $\boldsymbol{J}$ and using the definition of $\boldsymbol{A}$ as $\boldsymbol{B} = \boldsymbol{\nabla} \times \boldsymbol{A}$, we get a partial differential equation (PDE) for the magnetic field $\boldsymbol{B}$:

$$\boldsymbol{\nabla}^2 \boldsymbol{B} = \mu_0 \rho_s \boldsymbol{B} \tag{1.3}$$

The solution for the $1D$ case with boundary condition (BC) depicted in Fig. 1.3 is of the form: $B = B_0 e^{-\frac{x}{\lambda}}$. This exponential decaying of the magnetic field inside the bulk of a SC is called The Meissner Effect and it gives the relation between the SC stiffness and the penetration depth λ:

$$\rho_s = \frac{1}{\mu_0 \lambda^2} \tag{1.4}$$

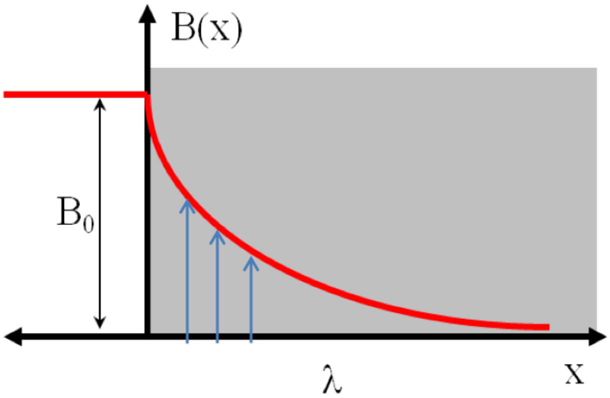

Figure 1.3: The Meissner effect - The magnetic field (red line) decays inside the SC interior (gray) on a length scale λ which called Penetration Depth.

The penetration depth (and hence the stiffness) is a temperature-dependent property - $\lambda(T)$ increases to infinity when the temperature approaches T_c. One can define the finite penetration depth at $T = 0$ as λ_0.

1.4 The Ginsburg-Landau Approach

The Ginsburg-Landau (GL) theory gives another way to describe superconductivity (following [3]). The theory impose a complex order parameter as the SC quantum macro state denoted as $\psi = |\psi|e^{i\phi} = \sqrt{n_s}e^{i\phi}$ where n_s is the charge carriers density. The GL functional of the free energy is given by (in CGS units):

$$f = f_{n0} + \alpha|\psi|^2 + \frac{\beta}{2}|\psi|^4 + \frac{1}{2m^*}|(\frac{\hbar}{i}\boldsymbol{\nabla} - \frac{e^*}{c}\boldsymbol{A})\psi|^2 + \frac{(\nabla \times \boldsymbol{A})^2}{8\pi} \tag{1.5}$$

Minimizing the free energy with respect to ψ^*, yields:

$$\alpha\psi + \beta|\psi|^2\psi + \frac{1}{2m^*}(\frac{\hbar}{i}\boldsymbol{\nabla} - \frac{e^*}{c}\boldsymbol{A})^2\psi = 0 \tag{1.6}$$

Minimizing with respect to $\boldsymbol{A}$ leads to:

$$\begin{aligned} \boldsymbol{J} &= \frac{1}{\mu_0}\boldsymbol{\nabla} \times \boldsymbol{\nabla} \times \boldsymbol{A} \qquad (1.7) \\ &= \frac{e^*\hbar}{2m^*i}(\psi^*\nabla\psi - \psi\nabla\psi^*) - \frac{e^{*2}}{m^*c}\psi^*\psi\boldsymbol{A} \\ &= \frac{e^*}{m^*}|\psi|^2(\hbar\boldsymbol{\nabla}\phi - \frac{e^*}{c}\boldsymbol{A}) = e^*|\psi|^2\boldsymbol{v}_s \end{aligned}$$

Where $\boldsymbol{v}_s$ is the charge carriers velocity, m^* is their mass, e^* is their charge and $|\psi_\infty|^2$ is their density deep inside the bulk of the SC. One can define $f = \psi/\psi_\infty$

and $\psi_\infty^2 = -\alpha/\beta > 0$ which minimize the free energy deep in the SC bulk where $\boldsymbol{A} = 0$ and $\boldsymbol{\nabla}\phi = 0$. Then if indeed there are no magnetic fields and $\boldsymbol{A} = 0$, Eq. 1.6 becomes (in the $1D$ case):

$$\frac{\hbar^2}{2m^*|\alpha|}\frac{d^2f}{dx^2} + f - f^3 = 0 \tag{1.8}$$

One can define the GL coherence length as:

$$\xi_{(GL)}^2 = \frac{\hbar^2}{2m^*|\alpha|} \tag{1.9}$$

When using $\frac{1}{2m^*}(\frac{\hbar}{i}\boldsymbol{\nabla} - \frac{e^*}{c}\boldsymbol{A})^2\psi = \frac{m^*v_s^2}{a}\psi$ in Eq. 1.6, we obtain:

$$|\psi|^2 = \psi_\infty^2(1 - \frac{m^*v_s^2}{2|\alpha|}) = \psi_\infty^2[1 - (\frac{\xi m^* v_s}{\hbar})^2] \tag{1.10}$$

$$J = e^*\psi_\infty^2(1 - \frac{m^*v_s^2}{2|\alpha|})v_s \tag{1.11}$$

One can see that J as a function of v_s gets a maximum for a specific velocity. Those are the critical current and the critical velocity:

$$J_c = e^*\psi_\infty^2\frac{2}{3}(\frac{2}{3}\frac{|\alpha|}{m^*})^{1/2} \tag{1.12}$$

$$v_c = (\frac{2}{3}\frac{|\alpha|}{m^*})^{1/2} \tag{1.13}$$

So if we measure the critical velocity v_c we can also find ξ using the relation:

$$\xi = \frac{\hbar}{\sqrt{3}m^*v_c} \tag{1.14}$$

Assuming that $m^* = 2m_e$ (m_e being the mass of a free electron) and $e^* = 2e$ (e being the charge of a free electron), one can extract from Eq. 1.5 that $\beta = |\alpha|\frac{8\pi e^2}{m_ec^2}\lambda^2$ and so $|\psi_\infty|^2 = \frac{m_ec^2}{8\pi e^2\lambda^2}$. Then using Eq. 1.12 we get:

$$J_c = \frac{m_ec^2}{6\pi e\lambda^2}v_c \tag{1.15}$$

And in MKS units:

$$J_c = \frac{2m_e}{3\mu_0 e\lambda^2}v_c \tag{1.16}$$

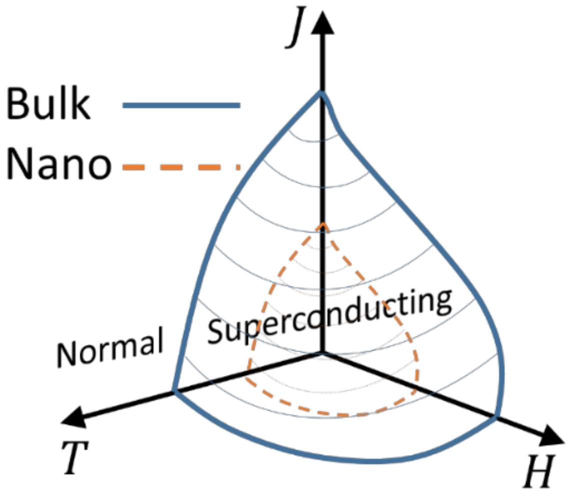

Figure 1.4: There is a dependency between the critical SC parameters, thus a critical surface (Blue) is created. In ultra-thin films, superconducting properties are suppressed and therefore create a shrinkage in the critical surface (Orange).

1.5 The Pearl Equation

In ultra-thin films, superconducting properties often deviate from their bulk counterparts [4, 5]. In particular, the superconducting energy gap (Δ) and the magnetic penetration depth (λ) can get strongly affected by the increased role of disorder [6], formation of vortex-antivortex pairs [7], and thermal phase fluctuations [8]. So indeed upon thinning the SC thickness d to get a thin film, there is a suppression of the critical temperature (T_c), the critical magnetic field (H_C) and the critical current (J_c) which creates a shrinkage of the critical surface on the SC phase diagram as illustrated schematically in Fig. 1.4

As was shown in section 1.3, a bulk of a SC material repels the magnetic field from its interior on a length scale called the penetration depth λ. The repulsion is due to SC currents density which flows close to the walls of the bulk that creates an opposite magnetic field which yields a zero total field in the interior. In a $2D$ SC film there no walls on which super-current density $\boldsymbol{J_s}$ can flow, therefore the magnetic field can easily penetrate and λ is increased in such a way that even a type-I SC becomes type-II ($\lambda > \xi$). However, there is still surface super-current density $\boldsymbol{\mathcal{J}_s}$ that can flow in the SC, therefore the relation between the vector potential $\boldsymbol{A}$ to $\boldsymbol{\mathcal{J}_s}$ can be defined as was shown by J.Pearl [9]. In the $2D$ case, the London equation becomes:

$$\boldsymbol{J_s} = -\frac{d}{\mu_0 \lambda^2} \boldsymbol{A} \delta\left(z\right) \tag{1.17}$$

The equation depicts a SC sheet of thickness d in the $z = 0$ plain. Taking Ampere's-Maxwell equation, placing the above expression for $\boldsymbol{J_s}$ and using the definition of $\boldsymbol{A}$ as $\boldsymbol{B} = \boldsymbol{\nabla} \times \boldsymbol{A}$, we get:

$$\boldsymbol{\nabla} \times \boldsymbol{\nabla} \times \boldsymbol{A} = -\frac{d}{\lambda^2} \boldsymbol{A} \delta\left(z\right) \tag{1.18}$$

Under the Coulomb gauge ($\nabla \cdot \boldsymbol{A} = 0$) and the definition of the new scale length $\Lambda = \frac{\lambda^2}{d}$ as the Pearl length, the Pearl equation is obtained:

$$\boldsymbol{\nabla^2} \boldsymbol{A} = -\frac{1}{\Lambda} \boldsymbol{A} \delta\left(z\right) \tag{1.19}$$

This equation characterized the vector potential $\boldsymbol{A}$ in the SC film and is governed by the Pearl length Λ which is a property of the film.

2 The Stiffnessometer

2.1 Principle of Operation

As was described in the previous chapter 1, the Stiffnessometer is a new measuring device that was developed [1] in our group to measure the superconducting stiffness ρ_s and the coherence length ξ of superconducting materials. The ideal Stiffnessometer is made out of an infinitely long conductive excitation-coil piercing a ring-shaped SC sample (for now, we will assume a bulk SC ring). Driving a current I through the conductive excitation-coil generates a uniform magnetic field inside the coil, parallel to its symmetry axis and zero magnetic field outside. Nevertheless, there is a vector potential $\boldsymbol{A_{coil}} = \frac{\Phi_{coil}}{2\pi r}\hat{\varphi} = \frac{\mu_0 n I \pi R^2}{2\pi r}\hat{\varphi}$ outside the coil, where n is the windings density and r is the distance from the coil's symmetry axis. A Zero-Gauge-Field-Cooling (ZGFC) is a process where the described setup of excitation-coil and SC ring is Cooled down below T_c in the absence of any magnetic field and zero vector potential $\boldsymbol{A_{tot}} = \boldsymbol{A_{coil}} + \boldsymbol{A_{ring}} = 0$, i.e without driving any current in the excitation coil. In this case, the SC will choose the phase ϕ to be such that the free energy will be minimized - given that $\boldsymbol{A_{tot}} = \boldsymbol{0}$ under ZGFC, the phase ϕ will be constant along the SC i.e, $\nabla\phi = 0$ and the familiar London equation- Eq. 1.2 is valid. furthermore, changing ϕ is energetically costly for the SC, so upon driving current I in the coil, the vector potential $\boldsymbol{A_{coil}} \neq 0$ anymore and super-currents $\boldsymbol{J}_s$ inside the SC ring will be formed (and therefore also a vector potential $\mathbf{A_{ring}}$) such that the relation $\boldsymbol{J}_s = -\rho_s \boldsymbol{A_{tot}}$ will be satisfied. Those super-currents going around in a loop create a magnetic moment m which can be measured using a pickup-loop connected to a SQUID. The London equation shows a linear relation between $\boldsymbol{J}_s$ and $\boldsymbol{A_{tot}}$. Since $\boldsymbol{A_{tot}}$ is proportional to the current I in the excitation coil, and $\boldsymbol{J}_s$ is proportional to the sample's magnetic moment m, we get a linear relation between the applied current and the measured signal. Therefore, one can extract the stiffness ρ_s. This linearity breaks down at some critical current I_c due to the fact that $\nabla\phi \neq 0$ anymore. One can measure the magnetic moment m in a constant temperature as a function of the current I and determines I_c and hence, the critical vector potential A_c, the critical current density J_c and the penetration depth ξ. Alternatively, one can measure the magnetic moment m in a constant current I (as long it is in the linear regime) at varying temperature and detect the stiffness as a function of the temperature. Both types of measurements will be described in detail in sections 2.3 and 2.4.

(a) (b)

Figure 2.1: (a) MPMS3 Stiffnessometer custom-made coil and sample holder. (b) Illustration of the excitation coil with a SC ring on it, the Gradiometer and the External Coil.

2.2 Experimental Setup

A major part of my experimental work was to implement the Stiffnessometer in an all-new QUANTUM DESIGN - MPMS3 Magnetometer that arrived at our group on Mar. 2019. The MPMS3 got a liquid He^4 cryostat with a base temperature of 1.8 [k]. All measurements presented in this work were taken in the MPMS3 Stiffnessometer. The implementation included fabrication of a custom-made coil and sample holder (Fig. 2.1a) that connects to a measurement rod with electrical wires in it. The excitation-coil that was used in all measurement is a 60 [mm] long, Cu double-layered coil with an external diameter of 0.8 [mm] and a total of 1940 windings. The ring-shaped SC sample is threaded onto the coil and placed in its center (Fig. 2.1a). The pickup loop is rather a second-order gradiometer. It is made of three winding groups. The outer two are made of two, clockwise winding loops each and the inner group is made of 4 loops winding anticlockwise (8 loops in total, as can be seen in Fig. 2.1b). The radius of the gradiometer is $R_{PL} = 8.5$ [mm]. Upon measuring, the gradiometer is static and fixed at $z = 0$, while the coil and the SC ring moving rigidly, altogether, up and down through it in the z direction. Therefore, the magnetic flux through the gradiometer is changing. An external coil is used to minimize the external magnetic field in the vicinity of the SC sample up to 10 [mG].

The gradiometer is connected to a SQUID that measures the change in the

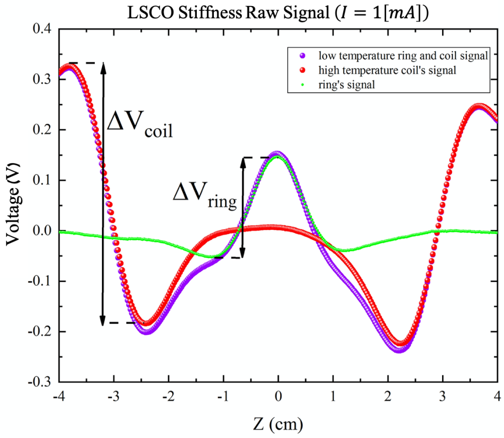

Figure 2.2: Stiffness measurements of LSCO ring with a current of $I = 1\,[\mathrm{mA}]$. During the measurements the ring and the excitation coil are moving along the z direction (the x-axis), in and out of the gradiometer which is fixed at $z = 0$. When they move, the magnetic flux through the gradiometer is changing, the SQUID measures the change and a corresponding output voltage is accepted (y-axis). Measuring below T_c (purple) yields a combined signal of the ring-shaped SC sample and the coil. Measuring above T_c (red) produce only the coil's signal because the ring doesn't have a superconducting response. By subtracting the coil signal from the combined signal we get the ring signal (green). ΔV_{ring} is the difference between the maximum and the minimum voltage of the ring signal and ΔV_{coil} is the same for the coil signal.

magnetic flux, based on the Josephson junction effect (JJE) and gives a corresponding voltage readout which is proportional to the magnetic flux through the gradiometer. The gradiometer's geometry yields a unique SQUID voltage output signal which is explained in detail in App. A.1. The output voltage of the MPMS3 can be translated to units of magnetic moment with a resolution of $\sim 10^{-11}\left[\mathrm{Am}^2\right]$. Fig. 2.2 presents such measurements of HTSC LSCO ring, above and below T_c. The coil contribution to the signal is obtained from the measurement above T_c. By subtracting the coil's signal from the total signal (measurement below T_c), we get the ring's signal. The difference between the maximum voltage and the minimum voltage of the ring's signal is defined as ΔV_{ring} and accordingly ΔV_{coil} is defined for the coil's signal. The measurable parameters ΔV_{ring} and ΔV_{coil} are proportional to the magnetic flux generated by the ring and coil respectively.

2.3 Thin Films Stiffness Measurement

The description of the stiffnessometer that was introduced up until now is valid also when measuring SC thin films. The only difference is that the supercurrents that are created in the ring satisfies the $2D$ London equation (Eq. 1.17). Following section 1.5, we get the Pearl equation for the stiffnessometer case and Eq. 1.19 then becomes:

$$\boldsymbol{\nabla}^2 \boldsymbol{A}_{ring} = \frac{1}{\Lambda}(\boldsymbol{A}_{coil} + \boldsymbol{A}_{ring})\delta(z) \tag{2.1}$$

Where $\Lambda = \frac{\lambda^2}{d}$ is the Pearl length, $\boldsymbol{A_{coil}} = \frac{\Phi_{coil}}{2\pi r}\hat{\varphi} = A_{coil}(R_{PL})\frac{R_{PL}}{r}\hat{\varphi}$ and due to the cylindrical symmetry $\boldsymbol{A_{ring}} = A_{ring}(r,z)\hat{\varphi}$. Upon normalization:

$$\begin{cases} \frac{r}{R_{PL}} \longrightarrow r \\ \frac{A_{ring}}{A_{coil}(R_{PL})} \longrightarrow A \\ \frac{\Lambda}{R_{PL}} \longrightarrow \Lambda \\ \frac{z}{R_{PL}} \longrightarrow z \end{cases} \tag{2.2}$$

We get the unit-less, normalized Pearl equation:

$$\nabla^2 A = \frac{1}{\Lambda}(\frac{1}{r} + A)\delta(z) \tag{2.3}$$

Because $\frac{1}{\Lambda} \rightarrow 0$ outside the SC ring, one can solve Laplace's equation:

$$\nabla^2 A = 0 \tag{2.4}$$

In the box $0 < z, r < L$ where $R_{PL} < L$ is the box side length (the solution is symmetrical in $\hat{\varphi}$). The ring is located at $z = 0$, $r_{in} < r < r_{out}$ and the following BC are obtained as a result of the jump condition in the magnetic field:

$$\begin{cases} \frac{\partial A}{\partial z} = \frac{1}{2\Lambda}\left(\frac{1}{r} + A\right) & z = 0\ ,\ r_{in} < r < r_{out} \\ \frac{\partial A}{\partial z} = 0 & z = 0\ ,\ 0 < r < r_{in} \\ \frac{\partial A}{\partial z} = 0 & z = 0\ ,\ r_{out} < r < L \\ A = 0 & else \end{cases} \tag{2.5}$$

We solved numerically the above PDE for different values of Λ, using finite elements method on the FreeFem $++$ software and confirmed the solution with Comsol $-$ 5.3a (calculated by Prof. Nir Gavish). From the numerical solutions, one can get the Pearl length as function of the solution in $r = R_{PL}$, $z = 0$, i.e $\Lambda(A(R_{PL}, 0))$ as presented in Fig. 2.3. As can be seen in the numerical solution,

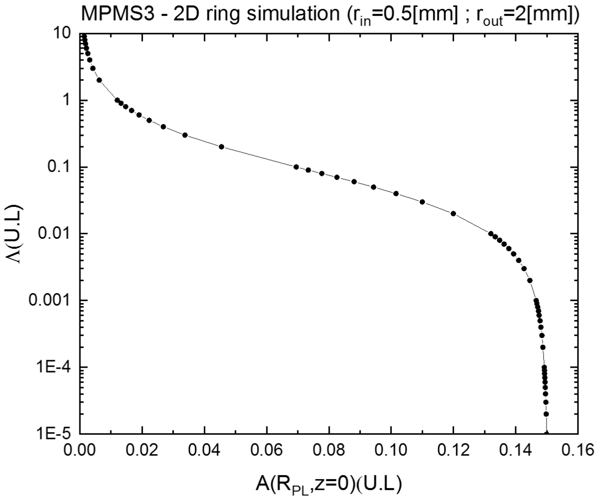

Figure 2.3: Numerical solution of the normalized Pearl equation (Eq. 2.3) for different Pearl lengths Λ and for ring size of $r_{in} = 0.5\,[\text{mm}]$ and $r_{out} = 2.0\,[\text{mm}]$. In the MPMS3 case, the radius of the gradiometer is $R_{PL} = 8.5\,[\text{mm}]$.

there are two saturated regions ($\Lambda < 0.001$ and $\Lambda > 10$) where small variations in $A\left(R_{PL}, 0\right)$ cause a big deviation in Λ. In this case, the Stiffnessometer method loses its sensitivity and it is not applicable anymore. Therefore, one can extract Pearl lengths of $0.001 < \Lambda < 10$ which are translated to penetration depth of in the range of $\lambda\,[\text{nm}] \in \left(60\sqrt{d}\,,\, 6000\sqrt{d}\right)$ where d is the film thickness given in [nm]. In App. A.2 properties of the Pearl equation numerical solution are shown.

As was already defined, $A\left(R_{PL}, z=0\right) = \frac{A_{ring}(R_{PL},z=0)}{A_{coil}(R_{PL})}$. Those vector potentials are proportional to the magnetic flux created by the SC ring and the coil, respectively, through a pickup-loop with radius R_{PL}, i.e., $\Phi_{coil} = \int \boldsymbol{B_{coil}} \boldsymbol{da} = \int \boldsymbol{A_{coil}} \boldsymbol{dl} = 2\pi R_{PL} A_{coil}\left(R_{PL}\right)$. On the previous section 2.2 we introduced the entities ΔV_{ring} and ΔV_{coil} (see Fig. 2.2). Had we used a single pickup-loop, we would be able to define ΔV_{coil}^{PL}, similarly, from the voltage as function of the displacement measurement. In this case the relation $\Delta V_{coil}^{PL} = k\Phi_{coil}$, where k is some proportionality factor is valid. Therefore, $\frac{\Delta V_{ring}^{PL}}{\Delta V_{coil}^{PL}} = \frac{A_{ring}(R_{PL},z=0)}{A_{coil}(R_{PL})}$. Since we use a gradiometer, there is a geometrical factor G that relates between the pickup-loop's voltages ratio and the gradiometer's voltages ratio. Therefore, in total:

$$V_{ratio} \equiv \frac{\Delta V_{ring}}{\Delta V_{coil}} = G\frac{A_{ring}(R_{PL}, z=0)}{A_{coil}(R_{PL})} = GA\left(R_{PL}, z=0\right) \qquad (2.6)$$

G can be found experimentally by using the saturation value of $\Lambda(A)$ or can be calculated directly, based on the geometrical factors of the gradiometer and the sample as shown in App. A.1.1. For the MPMS3 gradiometer, we found that $G \approx 3.18$ experimentally by measuring a high T_c SC ring- shaped LSCO sample as explained in App. A.1.2. One can now relates the voltage measurement to the normalized Pearl length by using the solutions of the normalized Pearl equation:

$$\Lambda\left(A\left(R_{PL}, z=0\right)\right) \longrightarrow \Lambda\left(\frac{V_{ratio}}{G}\right) \tag{2.7}$$

Multiplying the result by a R_{PL} factor will give the proper Pearl length. Since ΔV_{ring} is temperature dependent and so V_{ratio}, measuring from some base temperature all the way to some temperature above T_c will yields a $\Lambda(T)$ measurement which leads (by using the defintion $\Lambda = \frac{\lambda^2}{d}$, where d is the film thickness) to the penetration depth $\lambda(T)$ and the stiffness $\rho_s(T)$.

2.4 Thin Films Coherence Length Measurement

As was described in section 2.1, upon ZGFC the phase ϕ of the complex order-parameter will be constant along the SC ($\nabla\phi = 0$), due to free energy minimization. In that case, the relation $\boldsymbol{J}_s = -\rho_s \boldsymbol{A_{tot}}$ holds. Since $\boldsymbol{A_{tot}}$ is proportional to the current I in the excitation coil, and $\boldsymbol{J}_s$ is proportional to the sample's magnetic moment m, we get a linear relation between the applied current and the measured signal. This linearity breaks down in some critical current I_c since $\nabla\phi \neq 0$ anymore so the valid relation is given by the gauge-invariant London equation (Eq. 1.1). In thin SC films, the inhomogeneous phase can be translated to flux vortices that escape out from the center of the ring so, as will be shown in chapter 4, there are jumps in the ring's magnetic moment signal upon arriving at the critical current I_c.

To extract the coherence length ξ from the critical current, one needs to use the GL approach and to solve the minimization of the GL free energy. The work on this problem is in progress and done in a collaboration with Prof. Nir Gavish from the department of Mathematics in the Technion and Dr. Oded Kenneth from the Physics department. The GL free energy minimization yields coupled unitless PDE system under azimuthal symmetry assumption (giant vortex):

$$\begin{cases} \boldsymbol{\nabla}\times\boldsymbol{\nabla}\times A\hat{\theta} = -\frac{|\psi|^2}{\lambda^2}\left(A+\frac{J-l}{r}\right)\hat{\theta} \\ -\left|\psi\right|_{rr} - \frac{|\psi|_r}{r} - \left|\psi\right|_{zz} + \left(A+\frac{J-l}{r}\right)^2|\psi| = \frac{1}{\xi^2}\left(|\psi| - |\psi|^3\right) \end{cases} \tag{2.8}$$

Where J represents the number of flux quanta in the coil and l is an integer number representing the phase winding number. Fig. 2.4 presents numerical solutions for the total vector potential A_{tot} and the complex order-parameter

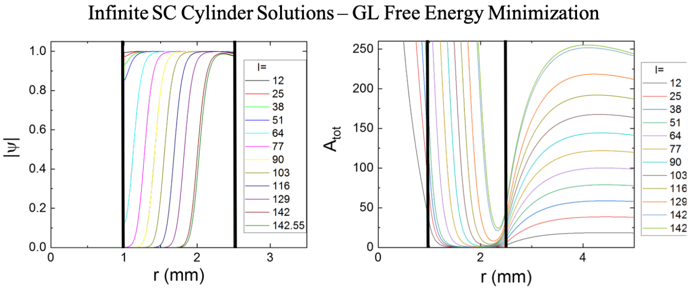

Figure 2.4: Numerical solutions of the normalized Pearl equation (Eq. 2.3) for different Pearl lengths Λ and for ring size of $r_{in} = 0.5\,[\text{mm}]$ and $r_{out} = 2.0\,[\text{mm}]$. In the MPMS3 case, the radius of the gradiometer is $R_{PL} = 8.5\,[\text{mm}]$.

amplitude $|\psi|$ for an infinite SC cylinder sample with different coil's current I (which is propotional and represented by J). This is not the case we deal with in our measurements but it gives the idea of what happens. Upon increasing J, the order-parameter starts weakened from the inner radius, in other words, the SC gives up the superconductivity in the inner parts in order to drive supercurrents on bigger loops and create an opposite magnetic flux more easily. In some critical current J_c, when the order-parameter weakening reaches the outer radius, $|\psi| \neq 1$ and $A_{tot} \neq 0$ at all points inside the SC and flux vortices can escape, i.e. there is a phase accumulation so $\nabla\phi \neq 0$.

From those results, we understand that the outer radius of the SC ring r_{out} plays an important role in the coherence length calculation, and indeed Oded Kenneth was able to show (work in progress), by solving analitically Eq. 2.8 close to J_c, that for the cases where $\xi \ll \lambda$, an elegant relation is accepted:

$$J_c \equiv \frac{\Phi_c}{\Phi_0} = \frac{r_{out}}{\xi} \tag{2.9}$$

Where Φ_0 is the magnetic flux quantum and Φ_c is the magnetic flux in the coil at the critical current I_c - for an infinite coil, the relation is given by:

$$\Phi_c = \mu_0 n \pi R^2 I_c \equiv \tilde{\Phi} I_c \tag{2.10}$$

Where n is the coil's windings density and R is its radius. Therefore, the coherence length is given by:

$$\xi = \frac{\Phi_0 r_{out}}{\tilde{\Phi} I_c} \tag{2.11}$$

For the double-layered Cu coil we used in all measurements, $\tilde{\Phi} = 1.031 \cdot 10^{-11}\,[\text{Wb/mA}]$ which is equivalent to $\frac{\tilde{\Phi}}{\Phi_0} = 4986\,\left[\text{mA}^{-1}\right]$.

3 Samples Fabrication

In this research work, the stiffness and coherence length measurements was done on polycrystalline $\delta - \mathrm{NbN}$ and granular Al films. Both materials are fabricated in a process of growing layers on top of Si substrate - the NbN films by a sputtering process and the granular Al films by thermal evaporation. As was described in the previous chapter 2, the Stiffnessometer method demands to work with ring-shaped SC films. Therefore, the first step is to fabricate an appropriate ring-shaped Si substrates. That was done by laser cutting a Si wafers on the ELAS Master Femto Laser System in Tel Aviv University Nanoscience Center with the help of Dr. Stanislav Stephanov. The ELAS laser system can emit ultra-short femtosecond laser pulses (down to $2.80 \cdot 10^{-13}$ [s]) that cause minimal heat-affected zone and maximize spatial precision. The main effort was to calibrate the laser parameters to get minimal surface damage. Fig. 3.1 presents a single ring-shaped Si substrate. The next fabricating step is to grow the SC film on the substrate.

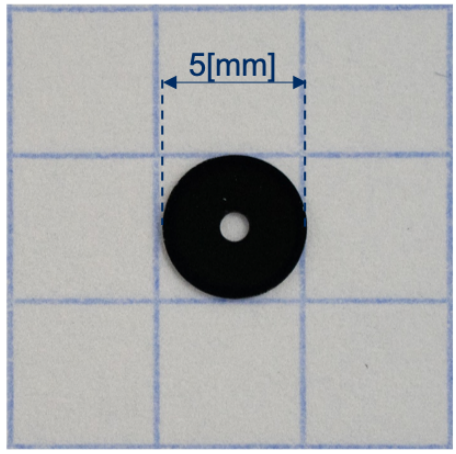

Figure 3.1: Ring-Shaped Si substrate that was laser cut in the ELAS Master Femto Laser System. the inner radius is $r_{in} = 0.5$ [mm] and the outer is $r_{out} = 2.5$ [mm]

3.1 NbN Ultra-Thin Films Fabrication

Niobium nitride (NbN) is a well known superconducting material with a relatively high bulk critical temperature $T_c \approx 16$[K] [10] compared to a pure Nb which presents a transition at $T_c \approx 9.2$[K] [10]. In recent years, NbN thin films have emerged as a popular material for fabricating sensitive superconducting bolometers capable of detecting up to a single photon. The ease of fabricating NbN films through magnetron sputtering and pulsed laser deposition, high

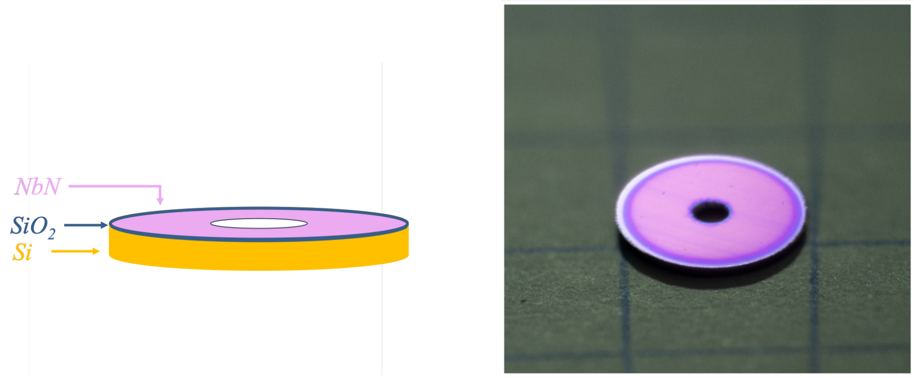

(a) (b)

Figure 3.2: (a) An illustration of the ultra-thin ring-shaped polycrystalline $\delta - \mathrm{NbN}$ film. The substrate is Si (yellow) with 300 [nm] thick $\mathrm{SiO_2}$ layer (blue). The NbN (pink) is sputtered on top of the oxide layer. (b) 3 [nm] thick Polycrystalline $\delta - \mathrm{NbN}$ ring-shaped film sputtered on Si (with 300 [nm] oxide layer) substrate. The inner radius is $r_{in} = 0.5\,[\mathrm{mm}]$ and the outer is $r_{out} = 2.0\,[\mathrm{mm}]$ which is smaller than the outer radius of the substrate (2.5 [mm]) due to the use of a circular ring holder that attaching the substrate to the heating plate during the sputtering.

transition temperature T_c, mechanical strength and chemical stability make it a material of choice for this application. As was described in section 1.5, superconductors usually suffer from miniaturization because their functional properties are suppressed with thickness reduction. Thanks to the relatively high T_c of bulk NbN, the functional properties of this material are maintained also at ultra-thin films ($< 5\,[\mathrm{nm}]$), i.e the T_c of 3 [nm] thick NbN film is $T_c \approx 7\,[K]$ which enables to conduct SC properties measurements on an He^4 cryostat such as in our MPMS3 magnetometer. The cubic phase is called $\delta - \mathrm{NbN}$ where Nb and N atoms are arranged alternatingly in a cubic lattice. That phase got a superior T_c relative to other phases and a bulk penetration depth of $\lambda_0 \approx 200\,[\mathrm{nm}]$.

Growing an ultra-thin NbN films with controllable properties is a non-trivial task because the SC properties deteriorate upon shrinking the SC thickness (Fig. 1.4). Thus, we used a sputtering fabrication process developed by Prof. Yachin Ivry and his student Itamar Holzman [11] from the Materials Engineering Faculty at The Technion to fabricate an ultra-thin ring-shaped polycrystalline $\delta - \mathrm{NbN}$ films on a Si substrate with a 300 [nm] thick $\mathrm{SiO_2}$ layer on top of it (Fig. 3.2a).

The sputtering itself was done by Dr. Guy Ankonina from the Technion Nano-center. The fabrication was carried out on ATC 2200 sputtering system (AJA International, Inc. USA) in a reactive DC magnetron setup. In the pro-

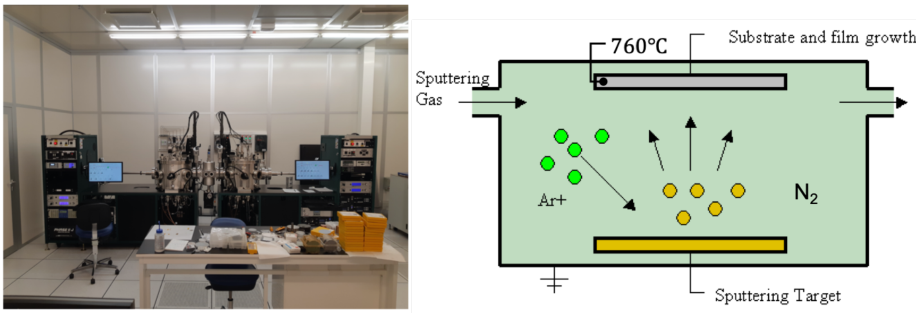

(a) (b)

Figure 3.3: (a) ATC 2200 sputtering system (AJA International, Inc. USA) in the clean-room of the Nano-center at the Technion where the NbN films fabrication took place. (b) Sputtering process illustration. A Nb target is bombarded by a mix of Ar : N_2 plasma which causing an ejection of Nb particles from the target that hits the Si substrate which is heated to 760°C to form a deposited $\delta-$NbN layer.

cess, a Nb target is bombarded by a mix of Ar : N_2 plasma causing an ejection of Nb particles from the target that hits the Si substrate to form a deposited layer. The desired $\delta-$NbN phase is not thermodynamically stable at room temperature. Hence, the ring-shaped Si substrate is heated while sputtering to 760°C. There are numerous control parameters for the sputtering procedure, changing each of them affects the deposition process and therefore the properties of the deposited layer, among them: the power applied on the Nb target, the partial pressure of the reactive gas (Ar : N_2), the substrate temperature and the deposition time. The applied power mainly affects the sputtering rate, while the partial pressure determines the deposited film composition. The substrate temperature affects the mobility of the deposited atoms and defines the crystallographic phase of the resulting film. Lastly, the deposition time determines the film thickness. The optimization and characterization process was carried out by Ivry's group [11], therefore the control parameters were already known and the NbN rings fabrication was done similarly according to them. Fig. 3.2b presents a 3 [nm] thick $\delta-$NbN ring-shaped film.

3.2 Granular Al Thin Films Fabrication

The Granular Al research was done in collaboration with Prof. Guy Deutscher and his student Aviv Glezer Moshe from the Tel Aviv University Physics department. Granular Al is a material composed of Al grains with a diameter on the order of $\varnothing \sim 1-10\,[\mathrm{nm}]$, separated by thin insulating barriers of Al oxide (Al_2O_3). The coupling between the grains can be controlled during film growth,

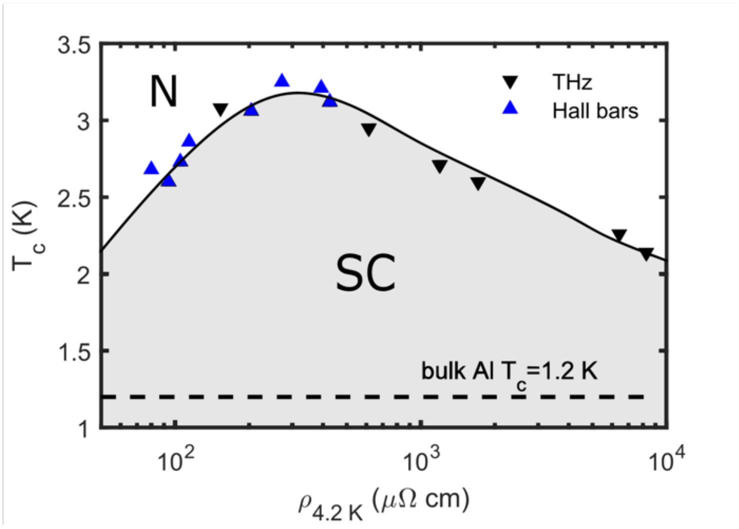

Figure 3.4: Granular Al phase diagram [13] - T_c vs room temperature resistivity which characterized the grains' coupling strength. The dashed line marks the bulk Al critical temperature $T_{c0} = 1.2\,[\mathrm{K}]$.

leading to samples with strong coupling and low resistivity (LR) in electrical transport, compared to high resistivity (HR) samples with weak intergrain coupling. In LR samples, T_c can be enhanced up to $3.2\,[\mathrm{K}]$ which is several times the bulk-value $T_{c0} = 1.2\,[\mathrm{K}]$, whereas it is suppressed in HR samples to form a superconducting dome in the phase diagram [12] (Fig. 3.4). Moreover, this confinement of electrons inside the nanoscale metallic grains reduces the value of the coherence length. Thereby, a BCS to BEC crossover is detected over changing the grains size [13].

The ring-shaped Granular Al films were fabricated in a thermal evaporation process by Aviv. That process includes heating a clean Al pallet in a vacuum chamber with base pressure of $\sim 1 \cdot 10^{-7}\,[\mathrm{Torr}]$ which cause evaporation of Al atoms that hit the Si ring-shaped substrate. The deposition is done in a controlled O_2 pressure while the substrate is cooled down to $\sim 77\,[\mathrm{K}]$ by a liquid nitrogen cold finger. Films with various degree of grain coupling were obtained by carefully varying the O_2 partial pressure in the range of $2\text{–}5 \cdot 10^{-5}\,[\mathrm{Torr}]$ and the deposition rate to about $5 \pm 1\,\left[\text{Å}/\mathrm{s}\right]$. Varying those parameters lead to different grains size distribution and therefore to different coupling. As was said earlier, the characterization of the samples is done by resistivity measurement at room temperature which indicates upon a strong or weak coupling of the grains.

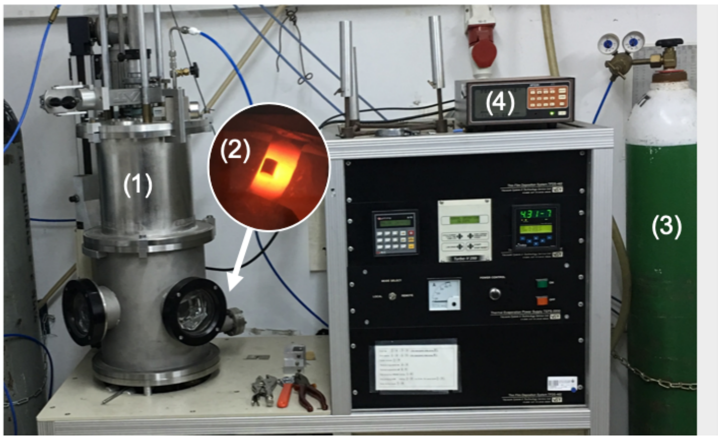

Figure 3.5: Granular Al thermal evaporation setup at Deutscher's lab at Tel Aviv University. (1) High vacuum chamber with a base pressure of $\sim 1 \cdot 10^{-7}$ [Torr] where the evaporation and deposition is done. The Al pallet sitts in the bottom of the chamber and the substrate is mounted on a cold finger in the upper part (2) Heated Al pallet. (3) The Oxygene source for evaporating in a controlled O_2 pressure. (4) Thickness monitor measures the frequency change of a piezoelectric sensor due to a mass accumulation.

4 Results & Data Analysis

4.1 Stiffness Measurements

4.1.1 NbN **Ultra-Thin Films:**

Fig. 4.1 presents the ring's signal (as described in section 2.2) of a 3 [nm] thick NbN film as a function of temperature. As can be seen, there is a surplus of SNR in this measurement which indicates that a reduction of factor 10 in the thickness of the samples is possible.

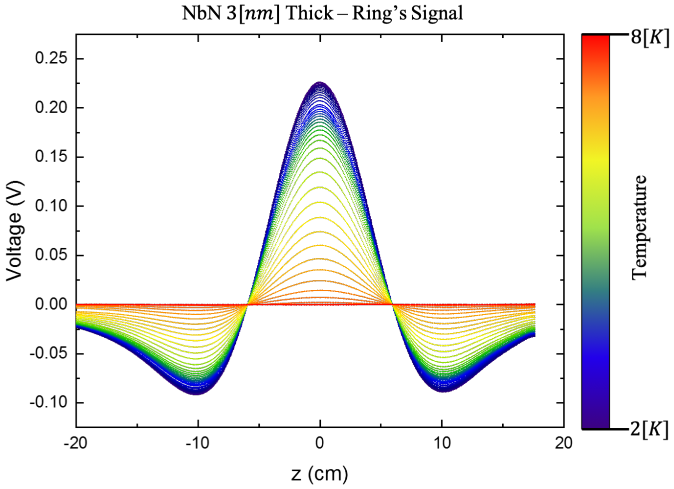

Figure 4.1: Ring's signal (described in section 2.2) of 3 [nm] thick NbN sample at various temperatures. The y-axis is the SQUID voltage and the x-axis is the displacement of the ring relative to the gradiometer center. As expected, upon increasing the temperature from the base temperature $T = 2$ [K], the signal of the SC is decreased until it vanishes above $T_c \approx 7$ [K].

Fig. 4.2 presents V_{ratio} measurements (described in section 2.2) of 3 [nm] and 5 [nm] thick NbN rings as function of the temperature. As can be seen, T_c is decreased with thickness. The temperature errors in all measurements conducted in this work are $\delta T \leq \pm 6 \cdot 10^{-3}$ [K].

Using the analysis described in section 2.3, we extracted the Pearl length as a function of the temperature $\Lambda (T)$ (Fig. 4.3a) and from it, by using the definition $\Lambda = \frac{\lambda^2}{d}$ where d is the film thickness, the stiffness $\rho_s \propto \lambda^{-2}(T)$ (Fig. 4.3b) and the penetration depth at the lowest temperature which gives an approximation for the penetration depth at $T = 0$ [K], i.e. λ_0. For the 5 [nm] thick NbN ring, we found that $\lambda (T = 2\,[\text{k}]) = 366 \pm 36$ [nm] and for the 3 [nm] thick NbN ring, $\lambda (T = 2\,[\text{k}]) = 602 \pm 20$ [nm].

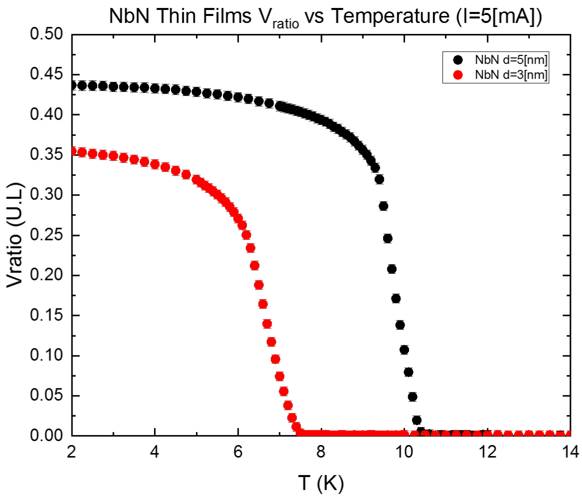

Figure 4.2: Stiffness measurements of 3 [nm] (red marks) and 5 [nm] (black marks) thick NbN rings as a function of the temperature for current $I = 5$ [mA]. The x-axis is the temperature in [k], and the y-axis is the ratio of the voltages $V_{ratio} \equiv \Delta V_{ring}/\Delta V_{coil}$ described in section 2.2.

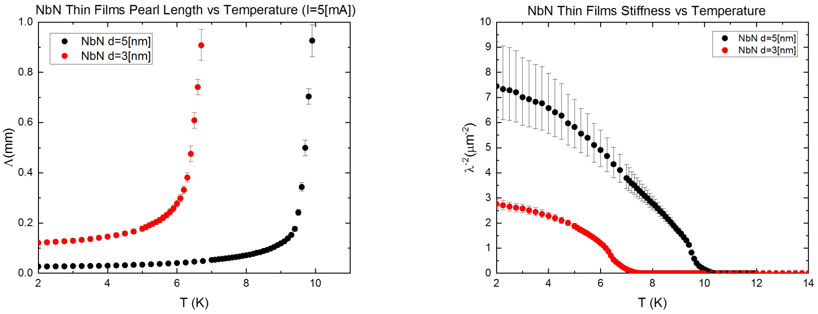

(a)

(b)

Figure 4.3: (a) The Pearl length Λ as a function of temperature for 3 [nm] (red marks) and 5 [nm] (black marks) thick NbN rings. (b) The Stiffness $\left(\rho_s \propto \lambda^{-2}\right)$ as a function of temperature for the same rings.

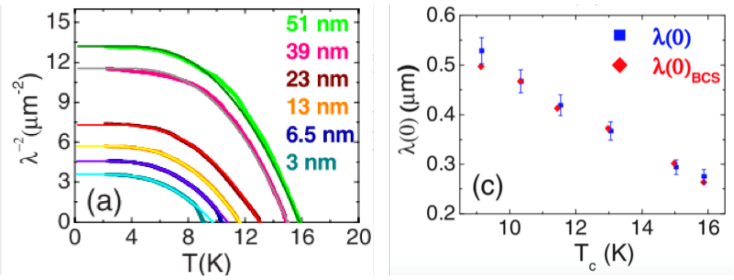

Figure 4.4: Epitaxial $\delta - $NbN thin films penetration depth measurements from various thicknesses using two coils mutual inductance technique [14]. The left figure presents the stiffness $\rho_s \propto \lambda^{-2}$ as a unction of temperature. The Right figure presents λ_0 as a function of T_c.

Comparing those results with a two coils mutual inductance measurements of epitaxial ultra-thin $\delta-$NbN films [14], we get a similar film-thickness dependency of T_c and the stiffness with a partial agreement on λ_0 - For a $3\,[\mathrm{nm}]$ thick $\delta - $NbN film, a penetration depth of $\lambda_0 = 529\,[\mathrm{nm}]$ was measured. Moreover, the stiffness temperature dependence is fundamentally different from ours - in the literature, the stiffness is temperature independent up to half of T_c while in the Stiffnessometer measurement, the dependency already arises from much lower temperatures.

4.1.2 Granular Al Thin Films:

Fig. 4.5 presents the same V_{ratio} measurements (with current $I = 5\,[\mathrm{mA}]$) for 3 different granular Al rings, which differ in their room temperature resistivity and their thickness (Table 4.1). T_c and the base-temperature V_{ratio} values are with inverse relation with the room temperature resistivity.

The same analysis was done as for the NbN films which yields the Pearl length as a function of the temperature $\Lambda(T)$ (Fig. 4.6a) and the stiffness $\rho_s \propto \lambda^{-2}(T)$ (Fig. 4.6b).

	Al-231019	Al-170919	Al-241019
Thickness $d\,[\mathrm{nm}]$	100	100	85
Room Temp. Resistivity $\rho\,[\mu\Omega\mathrm{cm}]$	238	310	810
Critical Temp. $T_c\,[\mathrm{K}]$	3.0	3.1	2.8
Penetration Depth $\lambda_0\,[\mu\mathrm{m}]$	1.38 ± 0.17	1.66 ± 0.16	2.36 ± 0.11
Coherence Length $\xi_0\,[\mathrm{nm}]$	10.08 ± 0.31	15.42 ± 0.53	14.04 ± 0.64

Table 4.1: Granular Al Samples

Fig. 4.7a presents the penetration depth at base temperature ($T = 1.8\,[\mathrm{K}]$) as function of room temperature resistivity in $[\mu\Omega\mathrm{cm}]$. For all granular Al samples

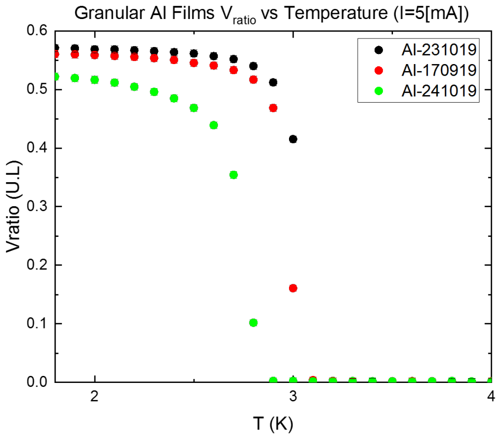

Figure 4.5: Stiffness measurements of 3 different granular Al rings (see Table 4.1) as a function of the temperature for current $I = 5\,[\mathrm{mA}]$. The x-axis is the temperature in [K], and the y-axis is the ratio of the voltages $V_{ratio} \equiv \Delta V_{ring}/\Delta V_{coil}$ described in section 2.2.

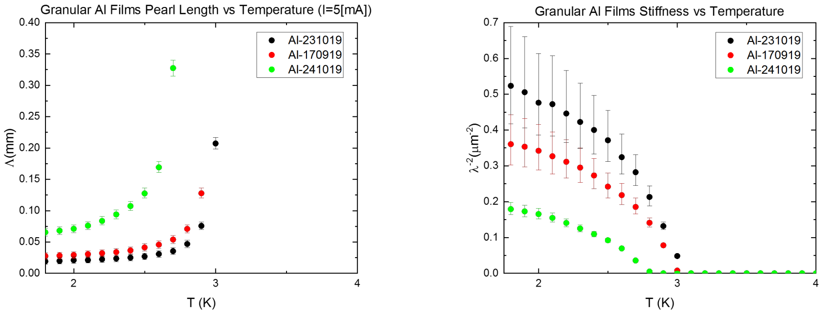

(a) (b)

Figure 4.6: (a) The Pearl length Λ as a function of temperature for 3 different granular Al rings, which differ in their room temperature resistivity and their thickness. (b) The Stiffness $\left(\rho_s \propto \lambda^{-2}\right)$ as a function of temperature for the same rings.

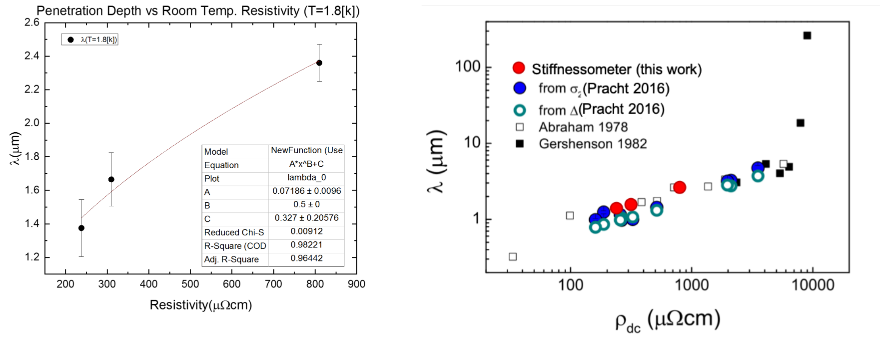

(a) (b)

Figure 4.7: (a) Granular Al penetration depth at $T = 1.8\,[\mathrm{K}]$ as a function of room temperature resistivity in $[\mu\Omega\mathrm{cm}]$. The fit presents a square root relation between those properties. (b) Penetration depth comparison with optical THz spectroscopy measurements [12].

measured, the penetration depth is in the order of $\lambda_0 \sim 1\,[\mu\mathrm{m}]$ (Table 4.1).

Comparing those results with optical THz spectroscopy measurements done on various granular Al films [12] (Fig. 4.7b), we get a significant agreement of the penetration depth's absolute values and the same square root dependency at the room temperature resistivity.

4.2 Coherence Length Measurements

4.2.1 NbN **Ultra-Thin Films:**

Fig. 4.8 presents ΔV_{ring} measurements (described in section 2.2) of $3\,[\mathrm{nm}]$ and $5\,[\mathrm{nm}]$ thick NbN rings as a function of the coil current I at the base temperature $T = 2\,[\mathrm{K}]$. As described in section 2.4, the critical current I_c is the lowest current for which the linearity between the ring magnetization (proportional to ΔV_{ring}) and the coil's vector potential (proportional to I) breaks. As can be seen, the critical current of the $5\,[\mathrm{nm}]$ thick NbN ring is $I_c = 44.5\,[\mathrm{mA}]$ and for the $3\,[\mathrm{nm}]$ is $I_c = 26\,[\mathrm{mA}]$.

Using the analysis described in section 2.4 and given that for both rings $r_{out} = 2.0\,[\mathrm{mm}]$, we extracted the coherence lengths according to Eq. 2.11 and found that $\xi = 7.07 \pm 0.36\,[\mathrm{nm}]$ for the $5\,[\mathrm{nm}]$ ring and $\xi = 10.84 \pm 0.66\,[\mathrm{nm}]$ for the $3\,[\mathrm{nm}]$ ring. Those results are with a good agreement to H_{C2} measurements of $10\,[\mathrm{nm}]$ NbN film which measured a coherence length of $\xi_0 = 6.5\,[\mathrm{nm}]$ [15].

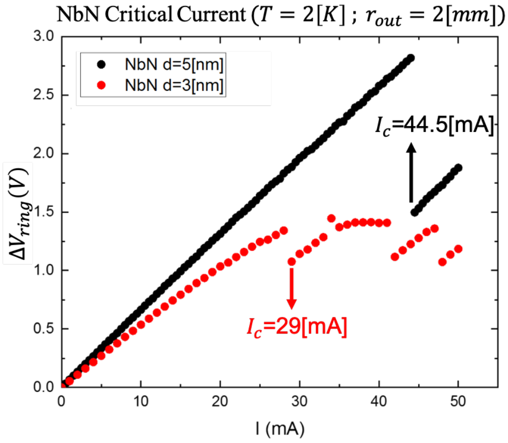

Figure 4.8: Critical current measurements of 3 [nm] (red marks) and 5 [nm] (black marks) thick NbN rings at the base temperature $T = 2$ [k]. the y-axis is ΔV_{ring} described in section 2.2 and the x-axis is the current I in the coil. The critical current of the 5 [nm] thick NbN ring is $I_c = 44.5$ [mA] and for the 3 [nm] is $I_c = 26$ [mA].

4.2.2 Granular Al Thin Films:

Fig. 4.9 presents similar ΔV_{ring} measurements for 3 different granular Al rings (Table 4.1) as a function of the coil current I at the base temperature $T = 1.8$ [K].

Using the analysis described in section 2.4 and given that for all rings $r_{out} = 2.5$ [mm], we extracted the coherence lengths according to Eq. 2.11. Fig. 4.10 presents the coherence length at the base temperature ($T = 1.8$ [K]) as a function of room temperature resistivity in [$\mu\Omega$cm] in comparison to H_{C2} measurements that were done on various granular Al samples by Aviv Glezer Moshe (work in progress - yet to be published). Our results give the same order of coherence lengths but yield a different behavior as a function of the resistivity.

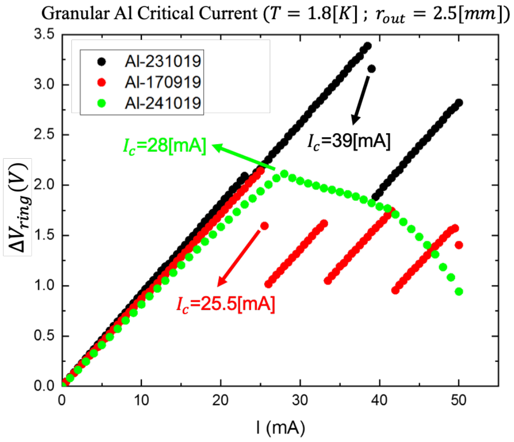

Figure 4.9: Critical current measurements of 3 different granular Al rings (see Table 4.1) at the base temperature $T = 1.8\,[\mathrm{K}]$. the y-axis is ΔV_{ring} described in section 2.2 and the x-axis is the current I in the coil.

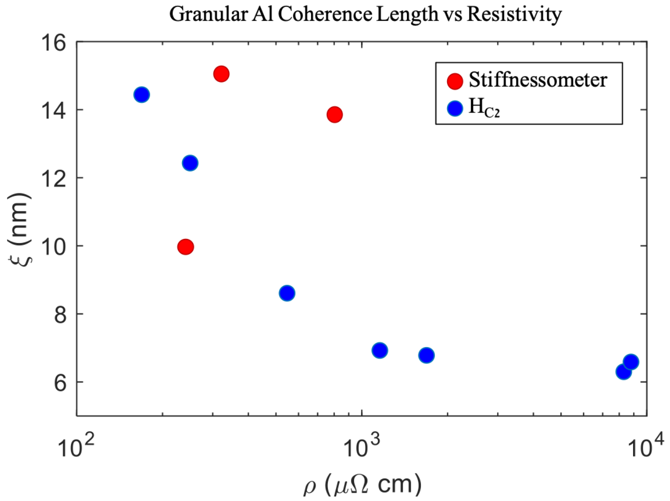

Figure 4.10: Comparison of Granular Al coherence lengths as a function of room temperature resistivity in $[\mu\Omega\mathrm{cm}]$. The Red marks are stiffnessometer measurements and the Blue marks are coherence lengths calculated from H_{C2} measurements done by Prof. Guy Deutscher and Aviv Glezer Moshe (work in progress - yet to be poblished).

5 Discussion

In this research work, we presented the Stiffnessometer and its ability to measure the penetration depth λ and coherence length ξ of ultra-thin SC films. Measurements of 3 [nm] thick polycrystalline $\delta-\text{NbN}$ film were introduced and proved that the Stiffnessometer indeed has the ability in terms of SNR and sensitivity to measure a true $2D$ SC systems such as in the case of a superconducting surface state of a TI induced by a proximity effect. Moreover, we measured different samples of polycrystalline $\delta-\text{NbN}$ and granular Al thin films and made a comparison with previous measurements done in known methods such as two coil inductance technique and optical THz spectroscopy. The comparison showed a good agreement with most of the measurement done in those known methods which validate the Stiffnessometer as a new method to measure thin SC films. The work presented so far could be published once we add few more films of NbN and improve the systematics of the granular Al results. Also, we have to understand why the temperature dependence of the stiffness measured by the Stiffnessometer is so different from other techniques. It might be that we need to solve the two coupled GL equations in 2D for analyzing the film data. This will require further theoretical development.

A Appendix

A.1 The Gradiometer G Factor

As was described in section 2.3, the geometrical factor G can be found experimentally by using the saturation value of $\Lambda\left(A\left(R_{PL}, z=0\right)\right)$ or can be calculated directly, based on the geometrical properties of the gradiometer and the sample. In this section, we will introduce both ways to calculate G.

A.1.1 G Calculation from Geometrical Properties

The SQUID signal is proportional to the total magnetic flux in the gradiometer which is the sum of the flux through each one of the 8 loops of the gradiometer. Those are arranged such that 4 loops with the same winding orientation are located in the center of the gradiometer and the other 4 loops have an oposite orientation and are split into two pairs. One is set 8 [mm] above the center and the other one is set 8 [mm] below (as can be seen in Fig. 2.1b). Therefore, the total flux is:

$$\Phi_{tot} = -2\Phi(z-8) + 4\Phi(z) - 2\Phi(z+8) \tag{A.1}$$

Where z is the displacement of the sample relative to the gradiometer center. In a way, the Φ_{tot} term have the structure of a second derivative of the total magnetic flux through a single pickup loop. The magnetic flux of a ring with magnetic moment m depends on the vector potential of the ring which is given by:

$$A_{ring}(R_{PL}, z) = \frac{2\pi m R_{PL}^2}{(R_{PL}^2 + z^2)^{\frac{3}{2}}} \tag{A.2}$$

The ratio between the total ring's vector potential on the gradiometer and the ring's vector potential on a single pickup loop at $z=0$ is:

$$\frac{A_{ring}^{Grad}(R_{PL}, z)}{A_{ring}^{PL}(R_{PL}, z=0)} = -\frac{2R_{PL}^3}{(R_{PL}^2 + (z+8)^2)^{\frac{3}{2}}} + \frac{4R_{PL}^3}{(R_{PL}^2 + z^2)^{\frac{3}{2}}} - \frac{2R_{PL}^3}{(R_{PL}^2 + (z-8)^2)^{\frac{3}{2}}} \tag{A.3}$$

The difference between the maximum and minimum of this function is:

$$\Delta\left(\frac{A_{ring}^{Grad}\left(R_{PL}\right)}{A_{ring}^{PL}(R_{PL}, z=0)}\right) = 3.173 \tag{A.4}$$

Similarly, we can define and manage the same process for the finite 60 [mm] long coil we used in the experiment and get:

$$\Delta\left(\frac{A_{coil}^{Grad}\left(R_{PL}\right)}{A_{coil}^{PL}(R_{PL}, z=0)}\right) = 1.1 \tag{A.5}$$

The voltage output is proportional to the sum of the flux through all 8 pickup loops of the gradiometer:

$$V(z) = K \cdot \Sigma_{PL} \int \boldsymbol{B}(z - z_{PL}) \cdot \boldsymbol{da} = K \cdot \Sigma_{PL} \int A(z - z_{PL}) \cdot dl$$

$$= K \cdot 2\pi R_{PL} A^{Grad}(R_{PL}, z) \tag{A.6}$$

Where K is a coefficient defined as $V = K \cdot \Phi_{PL}$. Therefore, one expects that:

$$\frac{\Delta V_{ring}}{\Delta V_{coil}} = 2.885 \frac{A^{PL}_{ring}(R_{PL}, z = 0)}{A^{PL}_{coil}(R_{PL}, z = 0)} \tag{A.7}$$

Following the definition of the G factor in section 2.3, one simply get that:

$$G = 2.885 \tag{A.8}$$

A.1.2 G Calculation from Saturation Value

In this work, we calculated the G factor experimentally by measuring a high T_c SC LSCO bulk sample (Fig. 1.1a). The extraction of the stiffness of a bulk SC (which is explained in details in the work of Dr. Itzik Kapon [1]) is done in a similar way to the thin films stiffness. The only difference is that the Pearl equation is not valid anymore (since $\lambda \ll d$) and one needs to solve the unitless $3D$-case PDE (instead of the normalized Pearl equation) with BC defined by the geometrical properties of the measured sample:

$$\nabla^2 A = \frac{1}{\lambda^2}(\frac{1}{r} + A) \tag{A.9}$$

Where $A \equiv \frac{A_{ring}}{A_{coil}(R_{PL}, z=0)}$, as was defined similarly in section 2.3. Fig. A.1 presents the solution of the PDE with the LSCO ring geometrical properties ($r_{in} = 0.5\,[\text{mm}]$, $r_{out} = 1.24\,[\text{mm}]$, $d = 1\,[\text{mm}]$) as a function of the penetration depth λ.

As can be seen, for penetration depth $\lambda < 0.01\,[\text{A.U}] \approx 0.1\,[\text{mm}]$ which satisfies $\lambda < d$ there is a saturation in the $A\,(R_{PL}, z = 0)$ value, i.e it's constant ($A^{sat}\,(R_{PL}, z = 0) = 0.161$) over a wide range of λ. And indeed, as can be seen in Fig. 1.1a, the V_{ratio} value saturates below T_c ($V^{sat}_{ratio} = 0.512$) since the penetration depth of the bulk LSCO sample is smaller than any other dimension. Therefore, one will require that:

$$\frac{V^{sat}_{ratio}}{G} = A^{sat} \quad \Longrightarrow \quad G = \frac{V^{sat}_{ratio}}{A^{sat}} = 3.18 \tag{A.10}$$

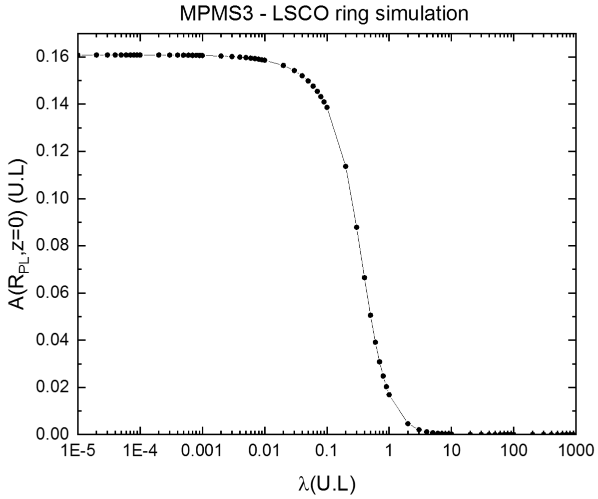

Figure A.1: Numerical solution of the normalized PDE (Eq. A.9) for different penetration depth λ and for ring size of $r_{in} = 0.5\,[\mathrm{mm}]$, $r_{out} = 1.24\,[\mathrm{mm}]$, $d = 1\,[\mathrm{mm}]$. The gradiometer radius of the MPMS3 is $R_{PL} = 8.5\,[\mathrm{mm}]$.

A.2 The Pearl Equation

In this short section, we will present two properties of the Pearl equation solutions (Eq. 2.3). Fig. A.2 shows that indeed the Pearl equation solution is the limit of the $3D$-case PDE solution (Eq. A.9) when the thickness of the SC sample d goes to zero while the other geometrical properties of the ring remain the same. This shows that the Pearl equation indeed describes the $2D$ case.

Fig. A.2 shows the dependency of the Pearl equation in r_{in} and r_{out}. One can see that the solution has a strong dependency on r_{out} while almost none on r_{in}. It can be explained by the fact that upon changing the outer radius, the vector potential changes more drastically because of the r^2 dependency of the flux. However, for all cases, the Λ sensitivity regions remain the same and yield the ability to detect penetration depth of $\lambda\,[\mathrm{nm}] \in \left(60\sqrt{d}\,,\, 6000\sqrt{d}\right)$. Having that and remembering that the $2D$ case is valid for $d \ll \lambda$, one can measure SC films with thickness up to $d = 360\,[\mathrm{nm}]$.

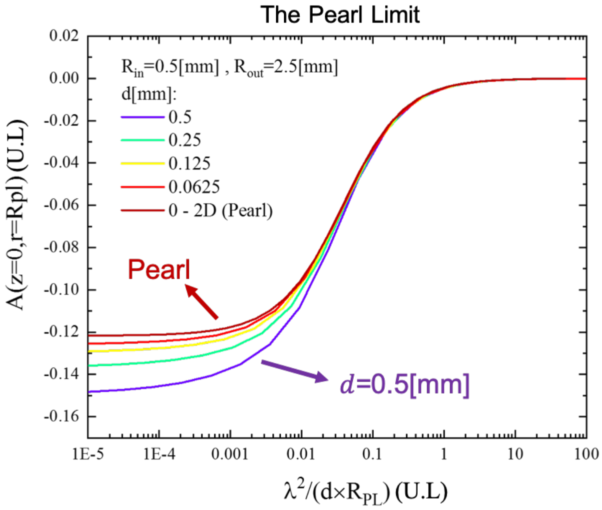

Figure A.2: The normalized vector potential $A\left(R_{PL}, z=0\right)$ as a function of the normalized Pearl length $\Lambda \equiv \frac{\lambda^2}{dR_{PL}}$. The Pearl equation solution is the limit of the $3D$-case PDE solution (Eq. A.9) when the thickness $d \to 0$ while $r_{in} = 0.5\,[\mathrm{mm}]$ and $r_{out} = 2.5\,[\mathrm{mm}]$ remains the same.

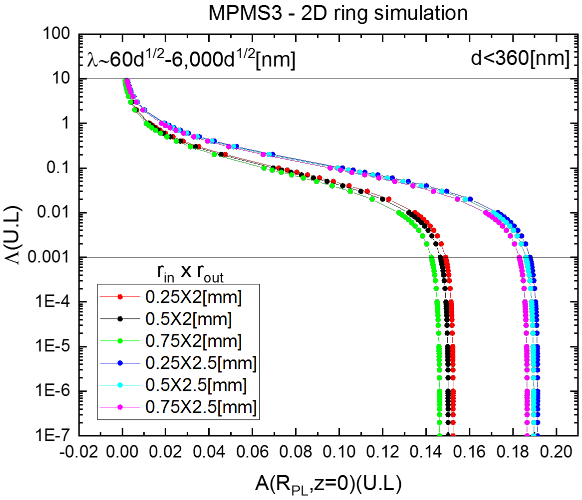

Figure A.3: The normalized vector potential $A\left(R_{PL}, z=0\right)$ as a function of the normalized Pearl length $\Lambda \equiv \frac{\lambda^2}{dR_{PL}}$ for different ring radii. The solution have a strong dependency on r_{out} while almost none on r_{in}

References

[1] I. Kapon, "Stiffnessometer, a magnetic-field-free superconducting stiffness meter and its application," in *Springer Theses* (Springer International Publishing, 2019) pp. 19–33.

[2] L. Fu and C. L. Kane, "Superconducting proximity effect and majorana fermions at the surface of a topological insulator," Physical Review Letters **100** (2008), 10.1103/physrevlett.100.096407.

[3] M. Tinkham, *Introduction to Superconductivity: v. 1* (Dover Publications Inc., 2004).

[4] Z. Wang, A. Kawakami, Y. Uzawa, and B. Komiyama, "Superconducting properties and crystal structures of single-crystal niobium nitride thin films deposited at ambient substrate temperature," Journal of Applied Physics **79**, 7837–7842 (1996).

[5] A. Semenov, B. Günther, U. Böttger, H.-W. Hübers, H. Bartolf, A. Engel, A. Schilling, K. Ilin, M. Siegel, R. Schneider, D. Gerthsen, and N. A. Gippius, "Optical and transport properties of ultrathin NbN films and nanostructures," Physical Review B **80** (2009), 10.1103/physrevb.80.054510.

[6] A. Finkel'stein, "Suppression of superconductivity in homogeneously disordered systems," Physica B: Condensed Matter **197**, 636–648 (1994).

[7] A. F. Hebard and A. T. Fiory, "Evidence for the Kosterlitz-Thouless transition in thin superconducting aluminum films," Physical Review Letters **44**, 291–294 (1980).

[8] S. J. Turneaure, T. R. Lemberger, and J. M. Graybeal, "Effect of thermal phase fluctuations on the superfluid density of two-dimensional superconducting films," Physical Review Letters **84**, 987–990 (2000).

[9] J. Pearl, "Current distribution in superconducting films carrying quantized fluxoids," Applied Physics Letters **5**, 65–66 (1964).

[10] B. T. Matthias, T. H. Geballe, and V. B. Compton, "Superconductivity," Reviews of Modern Physics **35**, 1–22 (1963).

[11] I. Holzman and Y. Ivry, "On-chip integrable planar nbn nanosquid with broad temperature and magnetic-field operation range," Appl. Phys. Lett. http://arxiv.org/abs/1904.07739v1 .

[12] U. S. Pracht, N. Bachar, L. Benfatto, G. Deutscher, E. Farber, M. Dressel, and M. Scheffler, "Enhanced cooper pairing versus suppressed phase coherence shaping the superconducting dome in coupled aluminum nanograins," Physical Review B **93** (2016), 10.1103/physrevb.93.100503.

[13] A. G. Moshe, E. Farber, and G. Deutscher, "Optical conductivity of granular aluminum films near the Mott metal-to-insulator transition," Physical Review B **99** (2019), 10.1103/physrevb.99.224503.

[14] A. Kamlapure, M. Mondal, M. Chand, A. Mishra, J. Jesudasan, V. Bagwe, L. Benfatto, V. Tripathi, and P. Raychaudhuri, "Measurement of magnetic penetration depth and superconducting energy gap in very thin epitaxial nbn films," Applied Physics Letters **96**, 072509 (2010), https://doi.org/10.1063/1.3314308 .

[15] D. Hazra, N. Tsavdaris, A. Mukhtarova, M. Jacquemin, F. Blanchet, R. Albert, S. Jebari, A. Grimm, E. Blanquet, F. Mercier, C. Chapelier, and M. Hofheinz, "The role of coulomb interaction in superconducting nbtin thin films," 10.1103/PhysRevB.97.144518, http://arxiv.org/abs/1711.04585v1 .

(Granular Al) בעלות מאפייני התנגדות שונים מעל הטמפרטורה הקריטית. השכבה הדקה ביותר שנמדדה הינה שכבת NbN בעובי של 3 ננומטר. יתירות של יחס אות לרעש במדידה זו מצביעה על היכולת למדוד שכבות דקות יותר ביחס 10 לשכבה זו, עובדה שתאפשר בעתיד למדוד מערכות דו־מימדיות בעלות שכבה חד אטומית.

עבודה זו מדגימה לראשונה שהקשיחומטר אכן תואם עם שיטות מדידה אחרות ופותח אפשרויות מדידה חדשות. בהשוואת ערכי הקשיחות הנמדדו באמצעות הקשיחומטר עבור האלומינום הגרעיני נמצאה התאמה מלאה לערכים בספרות שנמדדו בשיטת ספקטרוסקפיה בתחום ה־ THz של דגמים זהים. כמו־כן, מדידות אורך הקוהרנטיות של שני סוגי החומרים שנמדדו תואמות את הערכים המצויים בספרות.

תקציר

משוואת לונדון האינווריאנטית לכיול $\boldsymbol{J_s} = -\rho_s\left(\boldsymbol{A} - \frac{\hbar}{2e}\boldsymbol{\nabla}\phi\right)$ מעלה כי צפיפות הזרם העל מוליכה $\boldsymbol{J}_s$מתכונתית לפוטנציאל הוקטורי המגנטי $\boldsymbol{A}$ עד כדי גרדיאנט הפאזה של פרמטר הסדר המרוכב ϕ. קבוע הפרופרופורציה ρ_s מוגדר כקשיחות העל מוליכה ומקושר לעומק החדירה λ עפי המשואה $\rho_s = \frac{1}{\mu_o\lambda^2}$ והינו גודל התלוי בטמפרטורה של העל מוליך. ככל שמתקרבים לטמפרטורה הקריטית כך גדל עומק החדירה (ובהתאמה קטנה הקשיחות) עד להתבדרות מוחלטת במעבר אל מצב הצבירה הנורמאלי של החומר מעל הטמפרטורה הקריטית. כאשר מקררים על מוליך בהיעדר פוטנציאל וקטורי מגנטי $\boldsymbol{A}$, הפאזה ϕ תהיה אחידה בכל העל מוליך על מנת למזער את האנרגיה הקינטית. במקרים בהם ϕ מקוונטטת, היא נשארת קבועה גם בהגדלה מדודה של $\boldsymbol{A}$, מה שמוביל לקשר המבוטא במשוואת לונדון המוכרת $\boldsymbol{J_s} = -\rho_s\boldsymbol{A}$. קשר זה תקף עד אשר $\boldsymbol{J}_s$ מגיע לערך קריטי $\boldsymbol{J_c}$ שבו ϕ מאולצת להשתנות. אורך הקוהרנטיות ξ מתכונתי ל $\frac{1}{\boldsymbol{J_c}}$ותלוי בטמפרטורה גם כן. התהליך הסטנדרטי למדידת ρ_s בעל מוליך בעל נפח (תלת־מימדי) הינו הפעלת שדה מגנטי ומדידת עומק החדירה שלו אל פנים נפח העל מוליך. ברם, בשכבה על מוליכה דקה (דו־מימדית), עומק החדירה אינו מוגדר הייטב משום שלא קיים פנים נפחי. אף על פי כן, צפיפות הזרם העל מוליכה $\boldsymbol{J}_s$ ווקטור הפוטנציאל $\boldsymbol{A}$ אכן קיימים. שיטה חדשה למדידת הקשיחות העל מוליכה ואורך הקורלציה הנקראת "קשיחומטר" (Stiffnessometer) פותחה בקבוצת המחקר שלנו. שיטה זו מודדת את ρ_s ו־ $\boldsymbol{J_c}$ באופן ישיר על בסיס משוואת לונדון בנוכחות פוטנציאל וקטורי מגנטי ובהיעדר שדה מגנטי. טכניקה זו, התקפה עבור על מוליכים תלת־מימדיים ודו־מימדיים, מבוססת על שימוש בסליל־עירור צר וארוך העובר במרכז דגם על מוליך טבעתי ומשרה בה זרם על מוליך. המומנט המגנטי m של הטבעת נמדד באמצעות מגנטומטר סקוויד (מכשיר התאבכות קוונטית על־מוליכה ־ SQUID) על מנת לחלץ את ρ_s ו־ $\boldsymbol{J_c}$ (או את צפיפות הזרם המשטחי הקריטי $\boldsymbol{\mathcal{J}_c}$ במקרה הדו־מימדי). במקרה הדו־מימדי, חישוב הקשיחות העל מוליכה מתבצע עי פתרון משוואת פרל (Pearl) והשוואת התוצאה למדידות. חילוץ אורך הקוהרנטיות מתבצע עי ניתוח מלא של זוג משוואות גינצבורג ־ לנדאו (Ginzburg-Landau) המעלה את הקשר בין הזרם הקריטי המוזרם בסליל I_c לאורך ξ המבוקש.

לעבודת מחקר זו ישנן שתי מוטיבציות עיקריות. הראשונה היא לאשר שהערכים הנמדדים באמצעות הקשיחומטר תואמים ערכים הנמדדים בשיטות אחרות. בשל מגבלות רגישות השיטה במדידת עומק החדירה בכל סקלת הטמפרטורות (מטמפ הבסיס הנמוכה ביותר ועד לטמפ הקריטית) עבור דגמים תלת־מימדיים ישנו הצורך למדוד דגמים דו־מימדיים בהן אין מגבלת רגישות שכן עומק החדירה λ גדול מעובי הדגם d לכל טמפרטורה. המוטיבציה השניה הינה לבחון את יכולת הקשיחומטר למדוד שכבות על מוליכות דקות כהוכחת היתכנות לפרוייקט רחב יותר שמטרתו למדוד על מוליכות מושרת על מצבי שפה של מבודדים טופולוגיים המהווים מערכת על מוליכה דו־מימדית אמיתית.

בעבודה זו אציג את מדידות הקשיחות העל מוליכה ואורך הקוהרנטיות של מספר שכבות דקות של נאוביום ניטריד $\delta - \mathrm{NbN}$ בעלות עובי שונה ושל שכבות אלומינום גרעיני

המחקר נעשה בהנחיית פרופסור עמית קרן בפקולטה לפיזיקה

אני מודה לטכניון על התמיכה הכספית הנדיבה בהשתלמותי

מדידת הקשיחות העל מוליכה ואורך הקוהרנטיות של על מוליכים דו־מימדיים

חיבור על מחקר

לשם מילוי חלקי של הדרישות לקבלת התואר
מגיסטר למדעים בפיסיקה

ניצן בלאו

הוגש לסנט הטכניון ־ מכון טכנולוגי לישראל

טבת, התש"פ, חיפה, ינואר, 2020

מדידת הקשיחות העל מוליכה

ואורך הקוהרנטיות של על

מוליכים דו־מימדיים

ניצן בלאו